Progress in Natural Science: Materials International 32 (2022) 196–205

HOSTED BY

Contents lists available at ScienceDirect

Progress in Natural Science: Materials International

journal homepage: www.elsevier.com/locate/pnsmi

Phase formation, texture evolutions, and mechanical behaviors of $Al_{0.5}CoCr_{0.8}FeNi_{2.5}V_{0.2}$ high-entropy alloys upon cold rolling

Tongtong Sun [a], Weidong Song [b], Feilong Shan [a], Kaikai Song [a,b,*], Kun Zhang [c,**], Chuanxiao Peng [a], Honggang Sun [a], Lina Hu [d]

[a] School of Mechanical, Electrical & Information Engineering, Shandong University, 264209, Weihai, China
[b] State Key Laboratory of Explosion Science and Technology, Beijing Institute of Technology, 100081, Beijing, China
[c] CAS Key Laboratory of Microgravity (National Microgravity Laboratory), Institute of Mechanics, Chinese Academy of Sciences, 100190, Beijing, China
[d] Key Laboratory for Liquid-Solid Structural Evolution & Processing of Materials (Ministry of Education), Shandong University, 250061, Jinan, China

ARTICLE INFO

Keywords:
High-entropy alloys
Cold rolling
Texture
Mechanical property
Ductility

ABSTRACT

The cold rolling (CR) reduction dependence of microstructure evolutions and mechanical properties for $Al_{0.5}CoCr_{0.8}FeNi_{2.5}V_{0.2}$ high-entropy alloy (HEA) were investigated. The HEA remains FCC structures consisting of nanoscale ordered $L1_2$ phase, confirming the phase formation prediction. With increasing CR reduction, the textures transform from random ones to FCC rolling ones accompanied by dense slip bands and deformation twins. Under a 50% CR reduction, the deformation textures started to become evident and were governed by typical {111}<112>F, {110}<100>Goss and {112}<111>Cu texture components. When the CR reduction approached 90%, the deformation textures mainly contained the {110}<111>A, {114}<110>X, and {112}<111>Cu texture components. As a result, both Vickers hardness and ultimate strength increased, but the ductility decreased roughly. The enhanced strength should be attributed to the anisotropy and work hardening behavior from textures. The plastic deformation for the samples under low CR reductions was dominated by deformation twins and slip bands. However, under high CR reductions, the textures severely impeded the further propagation of pre-existing slip bands, leading to the rapid decrease of ductility. Therefore, the CR reduction should be carefully designed before optimal heat treatments to enhance the strength and ductility synergy.

1. Introduction

The engineering applications of metallic materials require comprehensive mechanical properties, i.e. high strength and good ductility [1–4]. Conventional metallic alloys, however, cannot always achieve this, particularly when the industrial requirements keep sustainable growth in today's society. Therefore, various advanced metallic materials have been developed using different state-of-art technologies [5–9]. Among them, the multiprincipal-component alloys or high-entropy alloys (HEAs) are expected to overcome this by their superior properties over their conventional counterparts in material properties, such as high strength and hardness, excellent high-temperature thermal stability, good corrosion resistance [10–17]. Generally, HEAs are defined as solid solution alloys that contain at least four principal elements in equal or near-equal atomic percent (at.%), and they are prone to form simple solid solutions such as FCC or BCC phases due to its higher mixing entropy [14–19]. By controlling alloying compositions and the thermo-mechanical processing, different heterogeneous HEA structures can be achieved to enhance the strength-ductility synergy [14–19]. By introducing single/multicomponent precipitate dispersions, bifunctional nanoprecipitates, heterogeneously structured nanoprecipitates, (chemical) short-range orders, coherent nanolamellar architectures, or herringbone-like hierarchical eutectic microstructure [20–27], not only the trade-off between strength and ductility is overcome but also other properties are also enhanced.

Among them, improving the content of one principal element in HEAs has been proven to be one of the most effective strategies to improve the mechanical properties of HEAs [28,29]. Until now, Ni-rich [30,31], Ti-rich [32], Mn-rich [33],Co-rich [34] HEAs have been explored. In particular, the Ni-rich type HEAs have drawn much research attention

* Corresponding author. School of Mechanical, Electrical & Information Engineering, Shandong University, 264209, Weihai, China
** Corresponding author.
E-mail addresses: songkaikai8297@gmail.com (K. Song), zhangkun@imech.ac.cn (K. Zhang).

https://doi.org/10.1016/j.pnsc.2022.01.008
Received 11 June 2021; Received in revised form 19 December 2021; Accepted 13 January 2022
Available online 19 January 2022
1002-0071/© 2022 Chinese Materials Research Society. Published by Elsevier B.V. This is an open access article under the CC BY-NC-ND license (http://creativecommons.org/licenses/by-nc-nd/4.0/).

due to their high strength and good ductility not only at room temperature but also at elevated temperatures [28,29,31,35–39]. For instance, by tailoring thermo-mechanical processing, an ultrafine-grained duplex microstructure in the $AlCoCrFeNi_{2.1}$ HEA [29] was achieved, which exhibits a good strength-ductility balance (yield strength: ~1.4 GPa, ductility: ~14%). Y.J. Liang et al. [28] introduced Ni_3Al-type ordered nano precipitates into a near-equiatomic disordered FCC matrix in $Al_{0.5}Cr_{0.9}FeNi_{2.5}V_{0.2}$ HEA, and the highest tensile strength was improved to be about 1.9 GPa together with a plastic strain of ~9%. A heterogeneous-structures-architecting strategy produced by cold rolling (CR) and intermediate-temperature-annealing [35] was also employed to overcome the strength-ductility trade-off in the $Al_{0.1}CoCrFeNi$, and the tensile strength and elongation of 982 MPa and 30.3% were obtained, respectively. Therefore, an increasing number of studies focus on the effect of medium- or high-temperature annealing/aging on the properties and the corresponding strengthening mechanisms of HEAs [28,29,31,35–46].

However, limited studies on the influence of texturing processing itself such as CR on mechanical properties of HEAs have been conducted. The importance of CR is that during deformation the work hardening effect will be raised, and the effects of defects such as shrinkage porosity or cavity can be effectively mitigated [47,48], and it can be one of the most important methods to guarantee mechanical properties of HEAs. Therefore, in this work the influence of the CR reductions on the microstructure evolutions especially the induced textures of Ni-rich $Al_{0.5}CoCr_{0.8}FeNi_{2.5}V_{0.2}$ HEA was investigated in detail. Additionally, the deformation mechanism and fracture features of the present HEA were also analyzed based on the experimental results.

2. Experiments

The ingots with a nominal composition of $Al_{0.5}CoCr_{0.8}FeNi_{2.5}V_{0.2}$ (at.%) were prepared by arc-melting a mixture of constituent elements (purity >99.9%) in a Ti-gettered high-purity argon atmosphere. During melting, the ingots were remelted at least five times to promote chemical homogeneity. Afterward, the molten alloy was suction-cast into a copper mold and then was subjected to the homogenization treatment at 1423 K for 24 h. The plates were subsequently cold rolled at room temperature using a custom-made CR equipment. The corresponding thickness reduction of CR was controlled to be 0%, 30%, 50%, 70%, and 90%, respectively. After CR, the samples were cut from the middle region of cold-rolled plates. The samples were then carefully ground and polished, and finally vibration-polished for the subsequent microstructure observations.

The phase formation and lattice parameters were characterized by X-ray diffraction (XRD, Rigaku D/max-rB, Cu K_α), Scanning Electron Microscopy (SEM, ZEISS Sigma500) equipped with an Electron Backscattered Diffraction system (EBSD Oxford Nordlys max3), and Transmission Electron Microscopy (Talos F200S G2). The microstructure evolutions before and after CR were characterized by an electron backscattered diffraction (EBSD Oxford Nordlys max3) at a sample title of 70°. The EBSD patterns were indexed according to the FCC Ni-superalloy as the base crystal and then the acquired date of EBSD was analyzed by the HKL Channel 5 software. TEM specimens were prepared by an ion beam thinner (Gatan PIPS II). High-Resolution TEM (HRTEM) investigations and selected area electron diffraction (SAED) patterns were adopted to characterize the formation of nanocrystals. The Vickers hardness values were measured by a Vickers hardness tester (Biaoyu HV-1000) under a load of 1.96 N for 10 s. The Vickers hardness of each sample was measured for six times at least. The tensile test was conducted using an electronic tensile testing machine at room temperature at an initial strain rate of $1 \times 10^{-3}\ s^{-1}$ along the rolling direction. The tensile samples are artificially machined into a dog-bone shape with a gauge length of 10 mm and a width of 3 mm by medium-speed wire-cut electrical discharge machining.

3. Results and discussion

3.1. Phase prediction and formation of HEAs

The phase formation of HEAs and its stability was predicted by valence electron concentrate (*VEC*) [49], the mixing enthalpy($\triangle H_{mix}$) [50], and mean square deviation of the atomic radii difference (δ) [50], respectively, which were calculated by

$$VEC = \sum_{i=1}^{n} c_i (VEC)_i \tag{1}$$

$$\Delta H_{mix} = 4\sum_{i=1, i\neq j}^{n} \Delta H_{i,j}^{mix} c_i c_j \tag{2}$$

$$\delta = \sqrt{\sum_{i=1}^{n} c_i (1 - r_i/\bar{r})^2} \tag{3}$$

where c_i is the atomic percentage, $(VEC)_i$ is the ith element *VEC*, $\Delta H_{i,j}^{mix}$ is the enthalpy of mixing between the ith and jth elements, and r_i is the ith element's atomic radius. According to Eq. (1), the *VEC* value of the $Al_{0.5}CoCr_{0.8}FeNi_{2.5}V_{0.2}$ HEA was determined to be ~8.2, while the $\triangle H_{mix}$ and δ were calculated via Eqs. (2) and (3) to be −7.1911 kJ/mol and 4.6%, respectively. It has been demonstrated that when the *VEC* is larger than 8, the HEAs belong to FCC-type alloys. Furthermore, as proven in Ref. [50], when $-15\ kJ/mol \leq \triangle H_{mix} \leq 5\ kJ/mol$ and $1\% \leq \delta \leq 6\%$, a single FCC solid solution is prone to form in HEA. Therefore, the FCC solid solutions trend to precipitate for this $Al_{0.5}CoCr_{0.8}FeNi_{2.5}V_{0.2}$ HEA.

Fig. 1(a) displays the XRD pattern of the homogenized $Al_{0.5}CoCr_{0.8}FeNi_{2.5}V_{0.2}$ HEA obtained at 1423 K for 24 h followed by quenching. Being consistent with the phase prediction and reported experimental results [49–52], only single FCC structures can be observed for the homogenized $Al_{0.5}CoCr_{0.8}FeNi_{2.5}V_{0.2}$ HEA. To confirm the microstructure features before CR, EBSD measurements were performed on the homogenized samples (Fig. 1(b–d)). Due to the very large grain size of the homogenized samples, only a few grains can be observed in the test field of vision. After homogenizing treatments, the dendritic chemical segregation of the as-cast $Al_{0.5}CoCr_{0.8}FeNi_{2.5}V_{0.2}$ HEA should be eliminated. The as-homogenized sample displays a typical coarse FCC equiaxed grain microstructure shown in Fig. 1(b), whose the average grain size located 826 ± 100 μm. The corresponding EBSD crystal-orientation map further confirms that there is no obvious grain orientation and other phases in the as-homogenized $Al_{0.5}CoCr_{0.8}FeNi_{2.5}V_{0.2}$ HEA (Fig. 1(c) and (d)).

Recently, Sistla et al. [51] have investigated the effect of Al/Ni ratio on the microstructure evolutions of $Al_xFeCoCrNi_{2-x}$ ($x = 0.3$ and 1) HEA, and the microstructure features display a strong dependence of the Al/Ni ratio especially of the Ni content. When decreasing Al/Ni ratio, the phase constitutes gradually changed as follows: (B2+α)→(B2+α+$L1_2$) →(FCC phase) →(FCC + B2) phases [51]. Dasari et al. [52] calculated the sectioned phase diagram at various constant molar quantities and also confirmed such experimental results. Hence, by tailoring alloy compositions or annealing treatments, different mixtures of FCC, BCC (B2), α or $L1_2$ phases can be achieved [52], leading to different mechanical behaviors. In order to confirm the presence of other nanoscale precipitates in the FCC matrix, the TEM measurements were conducted on the homogenized sample (Fig. 2). As shown in Fig. 2(a), the FCC phase is identified, while obvious diffraction pots related to superlattice from the SAED patterns also can be observed, implying the formation of the ordered FCC phase. Fig. 2(b) and (c) display the HRTEM and the corresponding SAED patterns. It is observed that the present FCC structures are composed of coherent nanoscale ordered ($L1_2$) precipitates in the disordered FCC matrix.

3.2. Microstructure features and textures upon cold rolling

When the CR reduction gradually increased from 0% to 90%, the phase-type of this HEA remained single FCC phase structures (Fig. 1(a)),

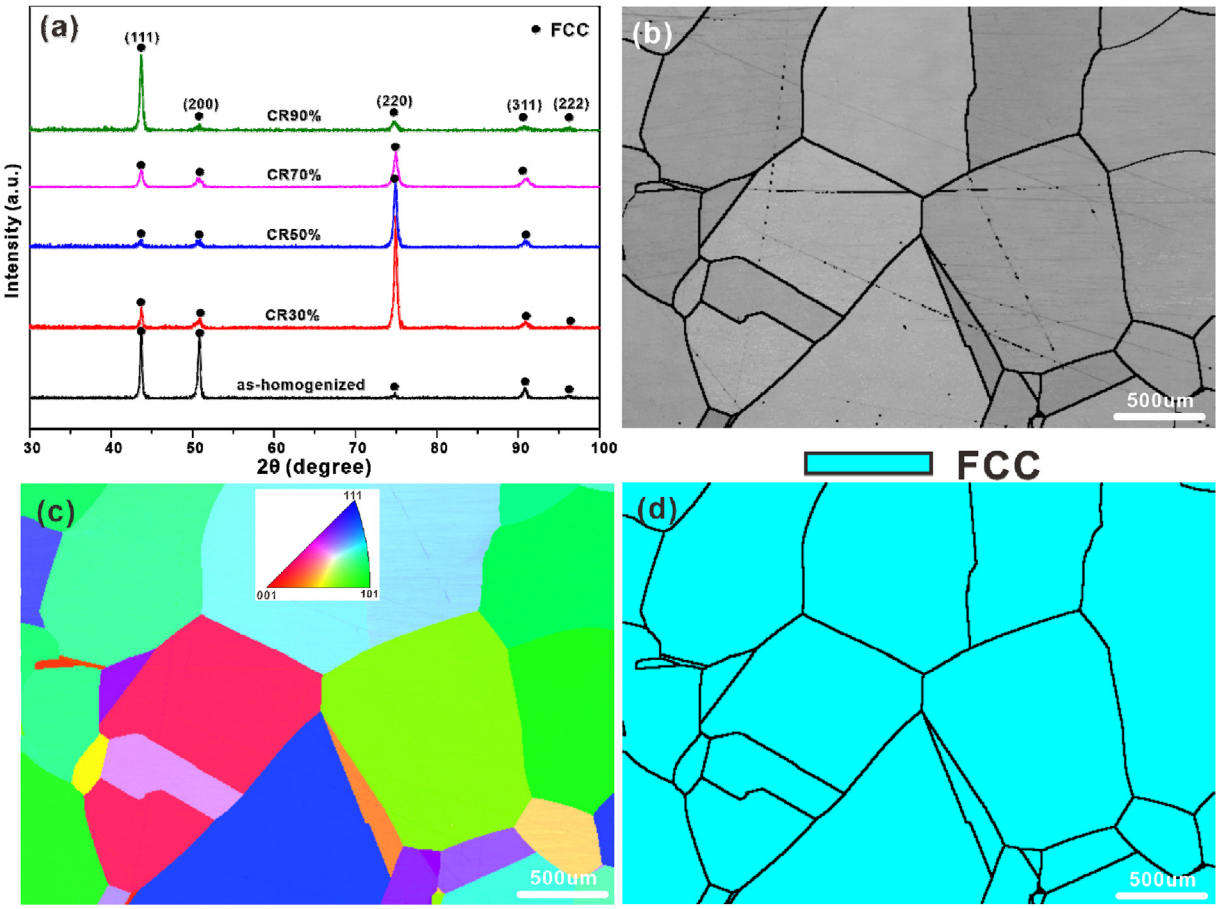

Fig. 1. (a) XRD patterns of the $Al_{0.5}CoCr_{0.8}FeNi_{2.5}V_{0.2}$ HEAs fabricated under different cold rolling conditions, and EBSD (b) image quality map, (c) crystal orientation map, and (d) phase map of the as-homogenized $Al_{0.5}CoCr_{0.8}FeNi_{2.5}V_{0.2}$ HEA.

while the density upon cold rolling gradually increased from 7.840 ± 0.05 g/cm^3 to 7.855 ± 0.10 g/cm^3. Furthermore, it has been demonstrated that the textures can be usually obtained after thermo-mechanical processing [53]. In the present study, the crystalline peak intensities of different lattice planes corresponding to the FCC phase also exhibited a remarkable change upon CR, indicating the possible formation of textures induced upon rolling (Fig. 1(a)).

In an attempt to confirm the microstructure features and texture evolutions upon CR, EBSD measurements were performed on the investigated samples, while the rolling direction-normal direction (i.e. RD-ND) plane is also displayed in Figs. 3–5. When the CR reduction gradually increased from 0% to 90%, the grains were gradually elongated along the RD direction, and then the deformed grains were parallel distributed along the rolling direction.

Compared with the CR 50% sample (Fig. 3), the grains of the CR 90% sample became longer and thinner (Fig. 4). On the one hand, a large number of dense slip lines appear within grains upon rolling (see dotted arrows in Figs. 3 and 4). During rolling, slip lines gradually extended over the whole grains and then stopped at the grain boundary due to the release of stress concentration, leading to the multiplication of deformation bands (Fig. 3). When the rolling process proceeds, multiple slip bands within grains may occasionally further develop along with the secondary or tertiary favorable orientation deformation [54]. As a result, some cross-distributed slip bands were also observed especially in the CR90% samples (Fig. 4). Meanwhile, more deformation bands around the grain boundaries gradually connect with each other and become obvious. Besides the rapid activation and development of multiple slip bands, some grains start to be broken down into tiny pieces due to the severe plastic deformation (Fig. 3(a–c) and 4(a-b)). The broken-down behavior becomes more obvious with increasing CR reduction. Besides broken grains, there were still large grains that exist in these rolled samples. Moreover, according to the EBSD crystal-orientation map of the CR50% and CR90% samples, a few lamellae-structured deformation twins also appear in some deformed grains especially for both samples (see solid arrows in Figs. 3 and 4).

On the other hand, according to the EBSD phase maps (Figs. 3(d) and 4(c)) for the samples under CR 50% and CR 90% reductions, no other phases could be observed, implying that there was no phase transformation occurring during the CR process. Meanwhile, as illustrated in the kernel average misorientation (KAM) maps (Figs. 3(e) and 4(d)), the high KAM areas were observed along grain boundaries and concentrated deformation bands. According to the strain gradient theory [55], the geometrically necessary dislocation (GND) density (Fig. 3(f) and insets in Fig. 4(d)) can be calculated according to the local misorientation angles. In general, the GND density can be increased with increasing plastic deformation due to inducing lattice curvature, which is developed by microstructure characteristics (e.g., grain size, texture) [56]. For both samples, the GND density can be roughly estimated to be ~9.4×10^{13} m^{-2} and ~2.5×10^{14} m^{-2}. Even though the total dislocation density is not equal to the GND density, the GND density can be used to qualitatively estimate the change tendency of the total dislocation density. In our case, with increasing CR reduction, the total dislocation density should be increased.

Furthermore, the detailed texture evolutions of the present alloys under CR 50% and CR 90% reductions were illustrated by constant φ_2 sections of the orientation distribution functions (ODFs) and the corresponding volume fractions of the main texture components (Fig. 5). As shown in Fig. 5(a) and (b), with increasing CR reduction, the induced

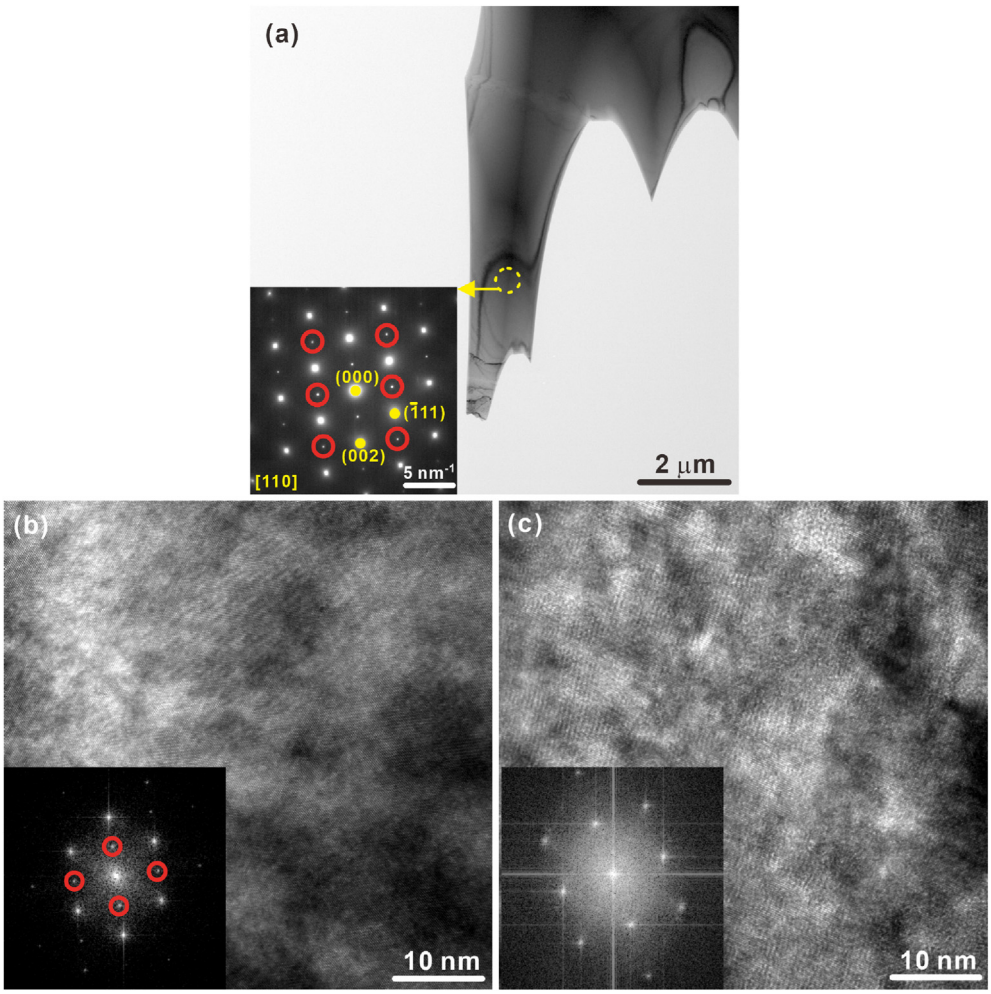

Fig. 2. (a) TEM image and SAED pattern of the as-homogenized $Al_{0.5}CoCr_{0.8}FeNi_{2.5}V_{0.2}$ HEA together with the HRTEM images and FFT patterns of the (b) ordered and (c) disordered regions.

textures gradually transform from the initially random ones to the FCC rolling ones [19,48,57]. Their definitions are given in Table 1. Under a CR 50% reduction, a large amount of deformation textures appear according to the constant $\varphi_2 = 45^\circ$ section of the orientation distribution functions (ODFs), which mainly consists of typical {111}<112>F, {110}<100>Goss and {112}<111>Cu texture components. Among them, the volume fraction of the {111}<112>F texture component is approximately 17.5% (Fig. 5(c)), while the intensity of the {110}<100>Goss texture is the highest.

At a low deformation level, the random orientation gradually becomes weak, and the plastic deformation is mainly governed by plane slip, leading to the formation of the Cu texture [57]. With increasing deformation levels, the deformation twins can be easily induced within the Cu component from the β-fiber texture, resulting in the appearance of the CuT orientation. When the CR reduction approaches 50%, the CuT texture component rotates to the Goss orientation G ({110}<001>) through the shear banding process [58,59]. However, for the CR 90% sample, the constant $\varphi_2 = 45^\circ$ section of the ODFs exhibits the appearance of the strong {110}<111>A, {114}<110>X, and {112}<111>Cu texture components. The volume fraction of the strong {110}<111>A texture component was about 10% (Fig. 5(c)), while the intensity of the {114}<110>X texture component was the highest. These observations imply that during server rolling deformation, the typical {111}<112>F and {110}<100>Goss texture components should be gradually replaced by the {110}<111>A and {114}<110>X ones. Previous studies [57] have demonstrated that the decrease of the F component from the β-fiber texture under a severe rolling deformation should be attributed to the severe planarity of dislocation slips and the rotation of twin lamellae.

3.3. Mechanical properties and deformation mechanism upon cold rolling

In an attempt to investigate the influence of textures on the mechanical properties of the present HEAs, the Vickers hardness devices and tensile tests were conducted, respectively. Fig. 6(a) shows the Vickers hardness of $Al_{0.5}CoCr_{0.8}FeNi_{2.5}V_{0.2}$ HEAs as a function of the CR reduction. The hardness of homogenized $Al_{0.5}CoCr_{0.8}FeNi_{2.5}V_{0.2}$ HEA was 262 ± 5 HV. With increasing CR reduction, the Vickers hardness gradually increased. After CR 90% reduction, the Vickers hardness was about two times higher than that of the homogenized state, and the hardness value was 570 ± 5 HV. Furthermore, the tensile properties were measured for the homogenized and rolled samples with different CR reductions along the RD direction, as shown in Fig. 6(b). The inset is the whole engineering stress-strain curves of the homogenized state, which presents an extremely large plastic strain of 45.3 ± 0.5% and a low yield strength of about 458 MPa (Fig. 6(b) and (c)). When the CR reduction gradually increased, the yield strength and tensile strength of this HEA increased significantly but the plasticity decreased. The yield strength, tensile strength, and fracture engineering strain of the CR 30% samples were 830 ± 10 MPa, 912 ± 7 MPa, and 11.1 ± 0.5%, respectively, exhibiting a good balance between strength and ductility (Fig. 6(b) and (c)). When the CR reduction increased to 90%, the yield strength raised to 1499 ± 5 MPa, which was ~3.27 times as much as the homogenized state (Fig. 6(b)

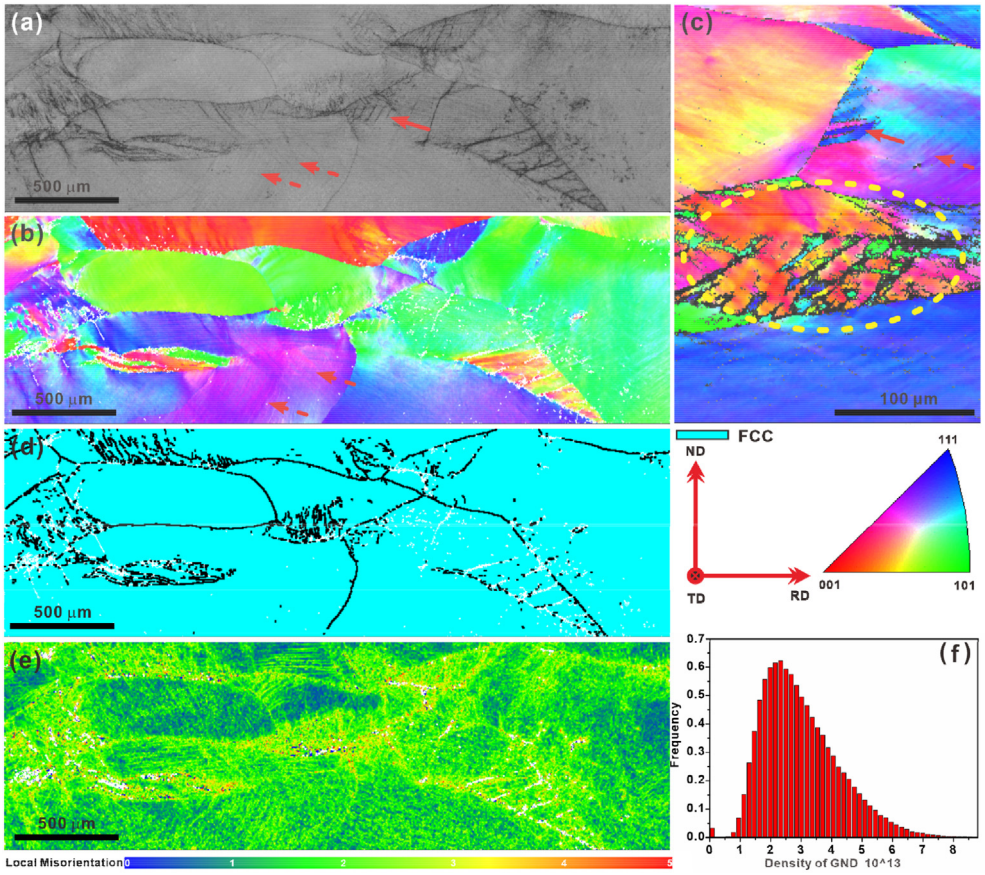

Fig. 3. EBSD (a) image quality map, (b) crystal orientation map and (c) its higher magnification, (d) phase map, (e) KAM map, and (f) the distribution of GND density of the CR50% HEA. The right-hand bottom corner consists of the rolling direction and the inverse pole figure, respectively.

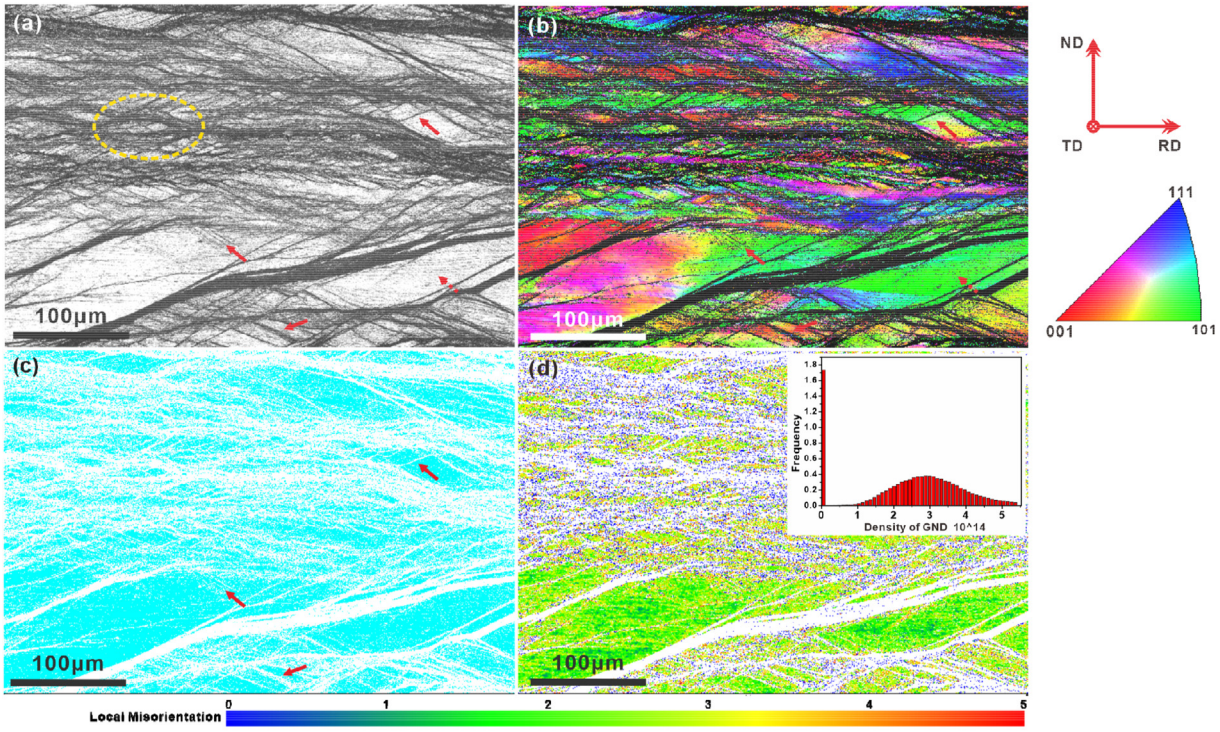

Fig. 4. EBSD (a) image quality map, (b) crystal orientation map, (c) phase map, and (e) KAM map (Inset: the distribution of GND density) of the CR90% $Al_{0.5}CoCr_{0.8}FeNi_{2.5}V_{0.2}$ HEA. The right-hand top corner consists of the rolling direction and the inverse pole figure, respectively.

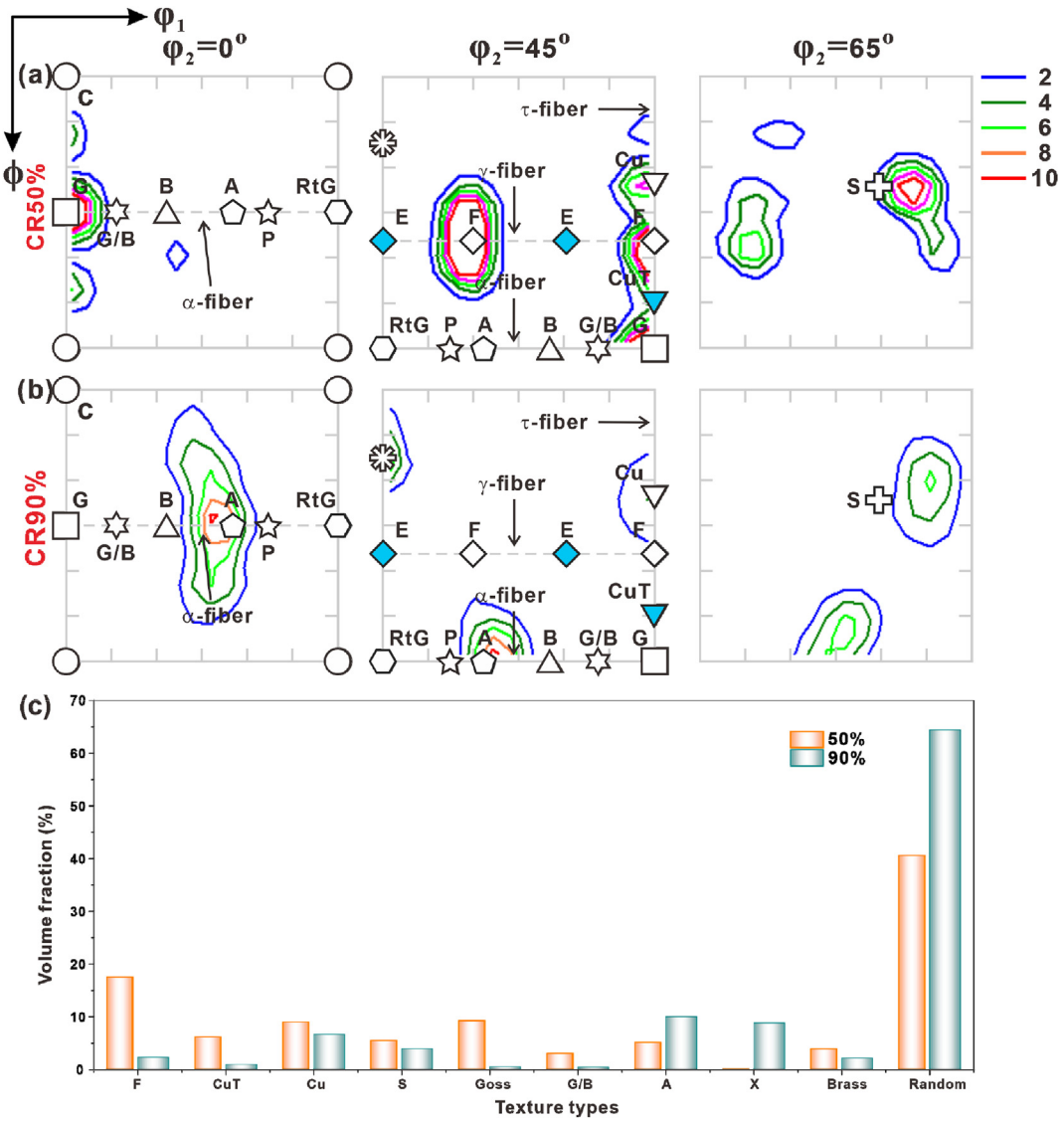

Fig. 5. Texture evolution i.e. ODF sections at φ_2 = 0°, 45°, and 65°, of the (a) CR50% and (b) CR90% HEAs, and (c) the volume fractions of the main texture components during cold rolling.

Table 1
Definition of texture components illustrated in Fig. 5.

Component	Symbol	Miller indices	Euler angles (φ_1, φ, φ_2)	Fiber
Brass (B)	△	{110} <112>	(55°,90°,45°)	α, β
Goss (G)	□	{110} <100>	(90°,90°,45°)	α, τ
Goss/Brass (G/B)	☼	{110} <115>	(74°,90°,45°)	α
Rotated Goss (RtG)	⬡	{110} <110>	(0°,90°,45°)	α
A	⬠	{110} <111>	(35°,90°,45°)	α
P	☆	{011} <211>	(30°,90°,45°)	α
Cube (C)	○	{001} <100>	(45°,0°,45°)	/
E	◆	{111} <110>	(0°/60°,55°,45°)	γ
F	◇	{111} <112>	(30°/90°,55°,45°)	γ
Copper (Cu)	▽	{112} <111>	(90°,35°,45°)	β, τ
CopperTwin (CuT)	▼	{552} <115>	(90°,74°,45°)	τ
S	✚	{123} <634>	(59°,37°,63°)	β
X	❁	{114} <110>	(0°,20°,45°)	
α-fiber	<110> parallel to ND			
β-fiber	<110> titled 60° from ND towards RD			
γ-fiber	<111> parallel ND			
τ-fiber	<110> parallel TD			

and (c)). The corresponding ultimate strength was ~2.17 times higher than that of the homogenized state (Fig. 7(b) and (c)). Moreover, with increasing CR reduction, the yield strength and ultimate strength increased almost linearly, and the maximum ultimate strength enhanced to be approximately 1528 MPa due to the work hardening effect and texture formation during rolling. However, the tensile ductility of the $Al_{0.5}CoCr_{0.8}FeNi_{2.5}V_{0.2}$ HEA decreased significantly to 2.6 ± 0.5% when the CR reduction increased to 70%. When the CR reduction increased from 70% to 90%, the plasticity was slightly improved from 2.6 ± 0.5% to 3.2 ± 0.5%.

Furthermore, as shown in Fig. 6(d), only a single FCC solid solution can be observed in the XRD patterns for the deformed samples, implying that there was not a solid phase transformation to appear during plastic deformation. Therefore, combined with the microstructure observations above, the gradually enhanced yield strength should be attributed to the lattice friction stress, grain boundary strengthening, precipitation strengthening, and the formation of the textures induced the anisotropy and work-hardening behavior. The yield strength can be roughly estimated by

$$\sigma_y = \Delta\sigma_{oc} + \Delta\sigma_{gb} + \Delta\sigma_{pr} + \Delta\sigma_{ds} + \Delta\sigma_{tx} \quad (4)$$

where σ_y is the yield strength, $\Delta\sigma_{gb}$, $\Delta\sigma_{pr}$, $\Delta\sigma_{ds}$, and $\Delta\sigma_{oc}$ are the strengthening contributions made by grain boundary, precipitation, dislocation, and texture, respectively. $\Delta\sigma_{oc}$ is the lattice frictional

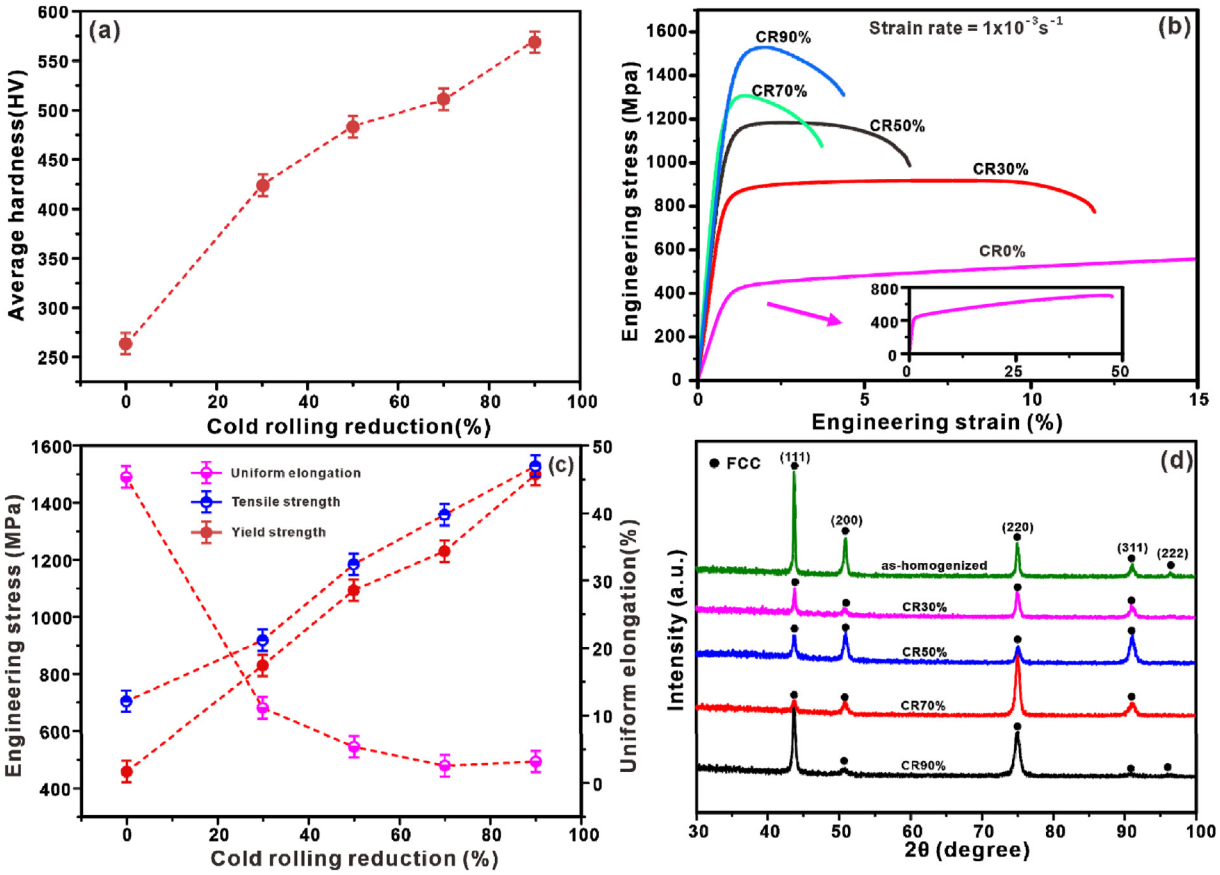

Fig. 6. (a) The Vickers hardness as a function of the CR reduction, (b) the engineering stress-strain curves under tension, (c) the correlation between the tensile strength, yield strength, and plastic strain, and XRD patterns of the $Al_{0.5}CoCr_{0.8}FeNi_{2.5}V_{0.2}$ HEAs fabricated under different CR reductions after fracture.

strength of the present alloy themselves. Meanwhile, $\Delta\sigma_{gb}$, $\Delta\sigma_{pr}$, and $\Delta\sigma_{ds}$ are usually estimated by the Hall-Petch relationship, the Orowan-Ashby equation, and Taylor equation [60,61], respectively. However, due to the existence of the textures strengthening, the $\Delta\sigma_{ds}$ should not be simply estimated by the Taylor equation since the interplay between dislocations-related strengthening mechanisms and textures is made via the Taylor factor for the critical resolved shear stress for slip [61]. In the present study a large amount of pre-existing dislocations (See GND density) were also induced upon CR and grouped into the wall at severe plastic deformation, which can act as the boundary of new grains. Meanwhile, strong grain fragmentation also occurred, which became more obvious with increasing CR reduction. Besides, nanoscale $L1_2$ precipitates could be observed in the disordered FCC matrix. As a result, during deformation the re-activation of dislocations and slip bands would be strongly restricted, leading to the improvement of yield strength with increasing CR reduction.

To further confirm the deductions above, the side surfaces were observed for the as-homogenized, the CR30%, CR 50%, CR70% and CR 90% alloys presented in Figs. 7–8. As shown in Fig. 7(a), there were two types of uniformly distributed fine slip lines with an angle of about 56.3° for the as-homogenized samples, and all these slip bands terminated around the grain boundary. During the deformation, the extended dislocations firstly nucleated from the intersections between grain boundaries and twinning boundaries (see solid arrows in Fig. 7(a–d)) [62], leading to the development of primary slip bands (Fig. 7(a) and (b)). With preceding deformation, the dislocation glide between the slip lines is easier than across the slip lines because the previously formed parallel slip lines and shear bands reduce the effective glide distance of dislocations along RD [54]. As a result, the devolvement of the secondary slip bands is further promoted and finally may lead to the formation of some sub-cracks perpendicular to the slip trace [63].

The same deformation behaviors also occurred in the CR 30% samples whose texture was not obvious (Fig. 7(c) and (d)). Therefore, for the CR 0% and CR 30%, it has been observed that the initial plastic deformation is still governed by the lanner slip and even cross-slip, while the later plastic deformation will be affected by deformation twins. During the initial plastic deformation, the dislocation shearing of the $L1_2$ nano precipitates leads to the predominant planar dislocation glide and the formation of crystallographically aligned slip bands as the main deformation mechanism. Moreover, the critical twinning stress strongly depends on the stacking fault energy [64]. The stacking fault energy of Ni-rich HEAs is usually between 35 mJ/m^2 and 60 mJ/m^2 [65], which belongs to a medium-to-high stacking fault energy. Therefore, only a limited number of deformation twins appear, which can still act as obstacles against the dislocation motion, reduce the mean free path, and then enhance the dislocation multiplications to some extent [66]. However, for the CR 70% and CR 90% samples, as shown in Fig. 7(e–h), the slip bands gradually extended from the accumulation at the grain boundaries to the penetration through the grain boundary, leading to the formation of a large number of obvious cracks (see solid arrows) near fracture. In such a case, a lot of pre-existing dislocations, slip bands, strong grain fragmentation, and obvious textures have existed for the CR 70% and CR 90% samples, a large number of grain boundary or boundary-like structures appear, which strongly impede the movement and propagation of new dislocations. Meanwhile, the texture induced the anisotropy and work hardening behavior during the CR process, and then the easy aviation of basal slip will be strongly restricted [67], leading to the enhancement of strength of the severely rolled samples. As a result, the continuous plastic deformation should be further released through the pre-existing slip bands, which are rapidly developed into micro-cracks, leading to work-softening and early fracture failure. When the CR reduction increased from 70% to 90%, the plasticity was slightly

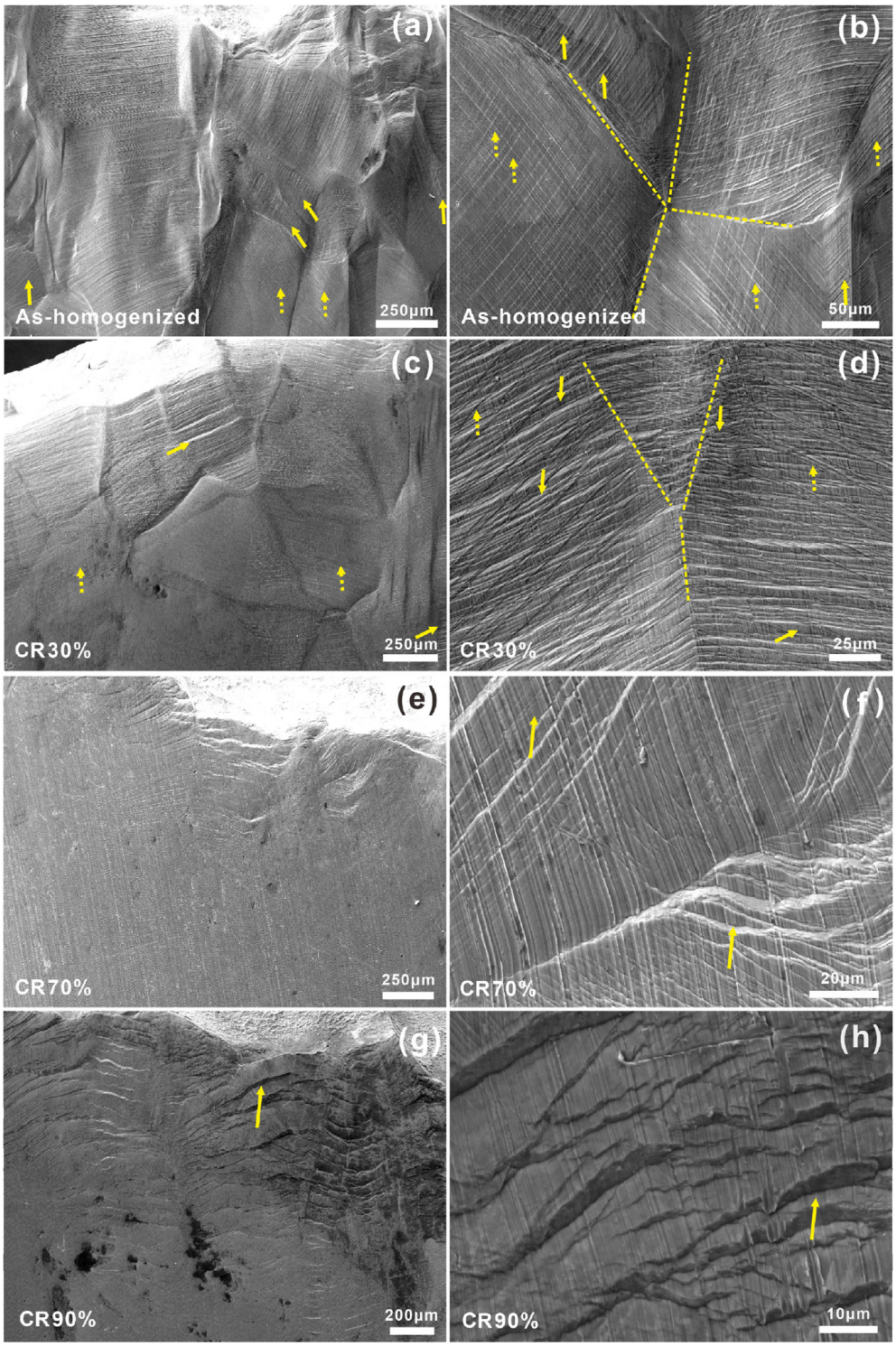

Fig. 7. SEM images of side surfaces after fracture for the $Al_{0.5}CoCr_{0.8}FeNi_{2.5}V_{0.2}$ HEAs: (a,b) the as-homogenized, (c,d) CR30%, (e,f) CR70%, and (g,h) CR90%.

improved from 2.6 ± 0.5% to 3.2 ± 0.5%, which should be due to partial grain breakage upon the severely plastic deformation.

For the samples obtained under the CR 50% reduction, the dense slip bands (see dotted arrows), a few deformation twins (see circles), and obvious cracks (see solid arrows) could be observed (Fig. 8(a) and (b)), which processes all the microstructure features during deformation mentioned for the homogenized and CR 90% samples. Therefore, the strength-ductility synergy in the present HEA can be effectively enhanced. Fig. 9 show the fracture morphologies of the HEA obtained under the CR 50% and 90% reductions. The fracture morphologies of the HEA obtained under the CR50% reduction were composed of many deep dimples (Fig. 9(a) and (b)), indicating that the fracture mode is typical dimple-rupture mode and belongs to the category of ductile fracture [68, 69]. When the CR reduction increased to 90%, there were many shallow dimple-like structures (Fig. 9(c) and (d)), indicating that the fracture surface after heavily rolling, the mode of fracture turned into shear-fracture mode [47,69,70].

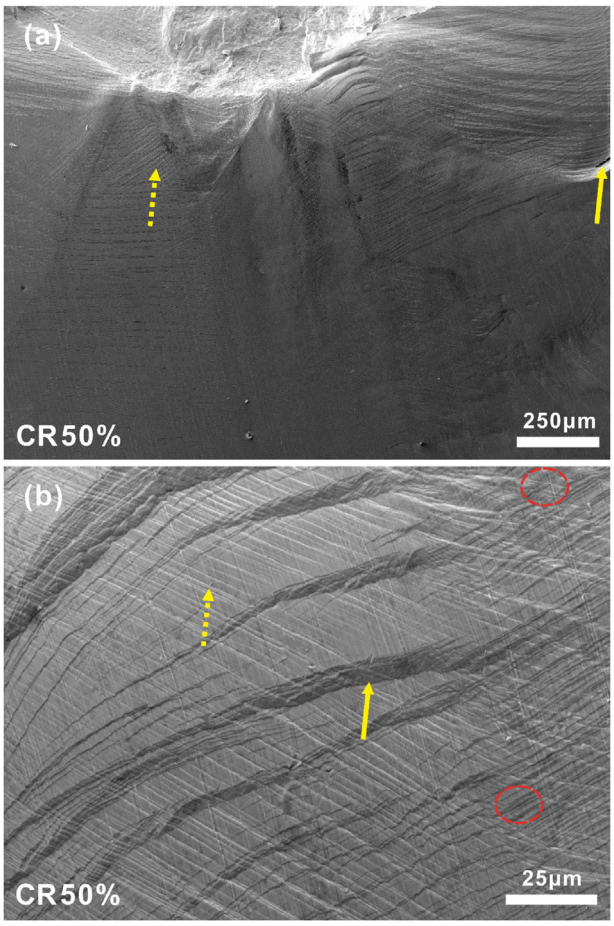

Fig. 8. SEM images of (a) side surfaces and (b) local regions after fracture for the CR50% sample.

4. Conclusions

The microstructure evolutions especially textures and the mechanical properties of Ni-rich $Al_{0.5}CoCr_{0.8}FeNi_{2.5}V_{0.2}$ HEA subjected to CR have been investigated in the present study.

(a) According to the prediction parameters (i.e. *VEC*, $\triangle H_{mix}$, and δ) related to phase formation of HEAs, the FCC solid solutions tend to precipitate in the $Al_{0.5}CoCr_{0.8}FeNi_{2.5}V_{0.2}$ HEA, which corresponds well to the experimental results. The homogenized sample displays a typical coarse FCC equiaxed microstructure, which consists of disordered and ordered ones. With CR proceeding, the present HEA remains the single FCC phase.

(b) With increasing CR reduction from 0% to 90%, the grains are gradually elongated along the rolling direction. Many dense slip lines appear and propagate within grains, and then stop at the grain boundary. With further deformation, the multiple slip bands within grains are occasionally developed, leading to the appearance of some cross-distributed slip bands, especially in the CR 90% samples. Meanwhile, some deformation twins also appear, and their number seems to be increased with proceeding deformation.

(c) The detailed texture evolutions are illustrated by constant φ_2 sections of the orientation distribution functions (ODFs). With increasing CR reduction from 0% to 90%, the textures transform from the random ones to the FCC rolling ones. Under a CR 50% reduction, the deformation textures mainly contain typical {111}<112>F, {110}<100>Goss and {112}<111>Cu texture components. When the CR reduction approaches 90%, the deformation textures mainly contain the {110}<111>A, {114}<110>X, and {112}<111>Cu texture components.

(d) Due to the existence of deformation textures, twins, and slip bands, the present alloy exhibits an excellent mechanical property. The corresponding Vickers hardness can be raised from 262 ± 5 HV to 570 ± 5 HV, while the maximum ultimate strength can be increased from 704 ± 5 MPa to 1528 ± 5 MPa. However, since

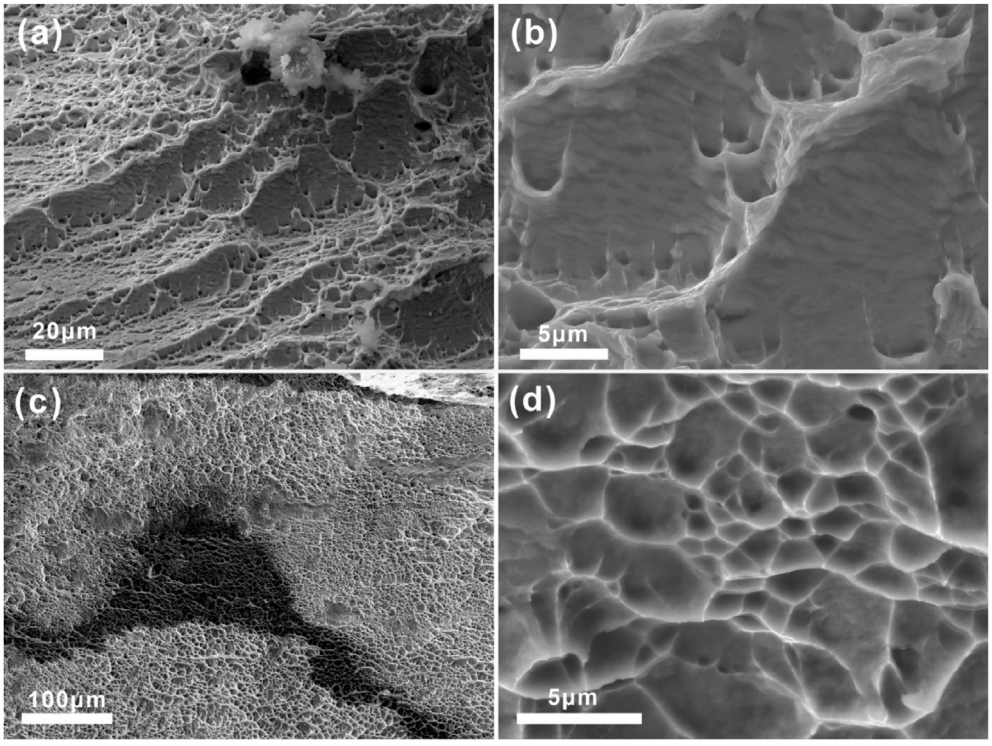

Fig. 9. SEM images of the fracture surfaces for the $Al_{0.5}CoCr_{0.8}FeNi_{2.5}V_{0.2}$ HEAs: (a,b) CR50%; (c,d) CR90%.

the activation of slip bands gradually becomes difficult with increasing rolling reduction, the tensile ductility decreases from 45.3 ± 0.5% to 3.2 ± 0.5%.

Declaration of competing interest

The authors declare that they have no known competing financial interests or personal relationships that could have appeared to influence the work reported in this paper.

Acknowledgments

The authors are grateful to K.L. Wang, and Y.Q. Xin for technical assistance. This research was funded by the National Natural Science Foundation of China (51871132 and 51971120) and the opening project of State Key Laboratory of Explosion Science and Technology (Beijing Institutes of Technology) (KFJJ21-08M).

References

[1] L. Liu, Q. Ding, Y. Zhong, J. Zou, J. Wu, Y.-L. Chiu, J. Li, Z. Zhang, Q. Yu, Z. Shen, Mater. Today 21 (2018) 354–361.
[2] J. Fan, L. Zhu, J. Lu, T. Fu, A. Chen, Scripta Mater. 184 (2020) 41–45.
[3] Z. Wang, S.Y. Tang, S. Scudino, Y.P. Ivanov, R.T. Qu, D. Wang, C. Yang, W.W. Zhang, A.L. Greer, J. Eckert, K.G. Prashanth, Addit. Manuf. 37 (2021) 101725.
[4] Y.F. Gao, W. Zhang, P.J. Shi, W.L. Ren, Y.B. Zhong, Mater. Today Adv. 8 (2020) 100103.
[5] W.H. Wang, Prog. Mater. Sci. 52 (2007) 540–596.
[6] A. Inoue, A. Takeuchi, Mater. Trans. 43 (2002) 1892–1906.
[7] W.L. Johnson, JOM 54 (2002) 40–43.
[8] W.E. Frazier, J. Mater. Eng. Perform. 23 (2014) 1917–1928.
[9] T.D. Ngo, A. Kashani, G. Imbalzano, K.T.Q. Nguyen, D. Hui, Composites Part B 143 (2018) 172–196.
[10] U. Sunkari, S.R. Reddy, B.D.S. Rathod, S.S.S. Kumar, R. Saha, S. Chatterjee, P.P. Bhattacharjee, Sci. Rep. 10 (2020) 6056.
[11] Y. Wang, M. Chen, F. Zhou, E. Ma, Nature 419 (2002) 912–915.
[12] Y.M. Wang, T. Voisin, J.T. McKeown, J. Ye, N.P. Calta, Z. Li, Z. Zeng, Y. Zhang, W. Chen, T.T. Roehling, Nat. Mater. 17 (2018) 63–71.
[13] Y. Zhang, T.T. Zuo, Z. Tang, M.C. Gao, K.A. Dahmen, P.K. Liaw, Z.P. Lu, Prog. Mater. Sci. 61 (2014) 1–93.
[14] M.H. Tsai, J.W. Yeh, Mater. Res. Lett. 2 (2014) 107–123.
[15] W. Zhang, P.K. Liaw, Y. Zhang, Sci. China Mater. 61 (2018) 2–22.
[16] D.B. Miracle, O.N. Senkov, Acta Mater. 122 (2017) 448–511.
[17] E.P. George, W.A. Curtin, C.C. Tasan, Acta Mater. 188 (2020) 435–474.
[18] F. Maresca, W.A. Curtin, Acta Mater. 182 (2020) 235–249.
[19] G.D. Sathiaraj, M.Z. Ahmed, P.P. Bhattacharjee, J. Alloys Compd. 664 (2016) 109–119.
[20] P. Shi, R. Li, Y. Li, Y. Wen, Y. Zhong, W. Ren, Z. Shen, T. Zheng, J. Peng, X. Liang, Science 373 (2021) 912–918.
[21] Q. Pan, L. Zhang, R. Feng, Q. Lu, K. An, A.C. Chuang, J.D. Poplawsky, P.K. Liaw, L. Lu, Science 374 (2021) 984–989.
[22] X. Chen, Q. Wang, Z. Cheng, M. Zhu, H. Zhou, P. Jiang, L. Zhou, Q. Xue, F. Yuan, J. Zhu, Nature 592 (2021) 712–716.
[23] L. Fan, T. Yang, Y. Zhao, J. Luan, G. Zhou, H. Wang, Z. Jiao, C.-T. Liu, Nat. Commun. 11 (2020) 6240.
[24] X. Du, W. Li, H. Chang, T. Yang, G. Duan, B. Wu, J. Huang, F. Chen, C. Liu, W. Chuang, Nat. Commun. 11 (2020) 2390.
[25] H. Luo, S.S. Sohn, W. Lu, L. Li, X. Li, C.K. Soundararajan, W. Krieger, Z. Li, D. Raabe, Nat. Commun. 11 (2020) 3081.
[26] R. Feng, Y. Rao, C. Liu, X. Xie, D. Yu, Y. Chen, M. Ghazisaeidi, T. Ungar, H. Wang, K. An, Nat. Commun. 12 (2021) 3588.
[27] T.J. Jang, W.S. Choi, D.W. Kim, G. Choi, H. Jun, A. Ferrari, F. Körmann, P.-P. Choi, S.S. Sohn, Nat. Commun. 12 (2021) 4703.
[28] Y.J. Liang, L. Wang, Y. Wen, B. Cheng, Q. Wu, T. Cao, Q. Xiao, Y. Xue, G. Sha, Y. Wang, Y. Ren, X. Li, L. Wang, F. Wang, H. Cai, Nat. Commun. 9 (2018) 4063.
[29] P. Shi, W. Ren, T. Zheng, Z. Ren, X. Hou, J. Peng, P. Hu, Y. Gao, Y. Zhong, P.K. Liaw, Nat. Commun. 10 (2019) 489.
[30] S. Wu, T. Yang, B. Cao, J. Luan, Y. Jia, L. Xu, Y. Mu, T. Zhang, H. Kong, X. Tong, Scripta Mater. 204 (2021) 114066.
[31] Z. Niu, Y. Xie, E. Axinte, J. Xu, Y. Wang, J. Alloys Compd. 846 (2020) 156342.
[32] L. Lilensten, J.-P. Couzinié, J. Bourgon, L. Perrière, G. Dirras, F. Prima, I. Guillot, Mater. Res. Lett. 5 (2017) 110.
[33] S. Huang, Z. Dong, W. Mu, V. Ström, G. Chai, L. Vitos, Appl. Phys. Lett. 117 (2020) 164101.
[34] B. Cao, H. Kong, Z. Ding, S. Wu, J. Luan, Z. Jiao, J. Lu, C. Liu, T. Yang, Scripta Mater. 199 (2021) 113826.
[35] S.W. Wu, G. Wang, Q. Wang, Y.D. Jia, J. Yi, Q.J. Zhai, J.B. Liu, B.A. Sun, H.J. Chu, J. Shen, P.K. Liaw, C.T. Liu, T.Y. Zhang, Acta Mater. 165 (2019) 444–458.
[36] A. Manzoni, H. Daoud, S. Mondal, S. van Smaalen, R. Völkl, U. Glatzel, N. Wanderka, J. Alloys Compd. 552 (2013) 430–436.
[37] L. Zhang, Y. Zhou, X. Jin, X. Du, B. Li, Mater. Sci. Eng. A 732 (2018) 186–191.
[38] Q.W. Tian, G.J. Zhang, K.X. Yin, W.L. Cheng, Y.N. Wang, J.C. Huang, Mater. Char. 176 (2021) 111148.
[39] Y. Lu, X. Gao, L. Jiang, Z. Chen, T. Wang, J. Jie, H. Kang, Y. Zhang, S. Guo, H. Ruan, Y. Zhao, Z. Cao, T. Li, Acta Mater. 124 (2017) 143–150.
[40] Q. Xiao, L. Wang, Y.-J. Liang, Y. Xue, Mater. Sci. Eng. A 801 (2021) 140403.
[41] C.-H. Tu, S.-K. Wu, C. Lin, Intermetallics 126 (2020) 106935.
[42] L. Zhang, X. Huo, A. Wang, X. Du, L. Zhang, W. Li, N. Zou, G. Wan, G. Duan, B. Wu, Intermetallics 122 (2020) 106813.
[43] Y.C. Huang, C.S. Tsao, S.K. Wu, C. Lin, C.H. Chen, Intermetallics 105 (2019) 146–152.
[44] C. Wei, Y. Lu, X. Du, J. Wang, T. Wang, Mater. Sci. Eng. A 805 (2021) 140548.
[45] S.W. Wu, L. Xu, X.D. Ma, Y.F. Jia, Y.K. Mu, Y.D. Jia, G. Wang, C.T. Liu, Mater. Sci. Eng. A 805 (2021) 140523.
[46] X. Huang, J. Miao, S. Li, C.D. Taylor, A.A. Luo, J. Mater. Sci. 56 (2021) 7670–7680.
[47] J. Hou, M. Zhang, S. Ma, P.K. Liaw, Y. Zhang, J. Qiao, Mater. Sci. Eng. A 707 (2017) 593–601.
[48] G.D. Sathiaraj, A. Pukenas, W. Skrotzki, J. Alloys Compd. 826 (2020) 154183.
[49] S. Guo, C. Ng, J. Lu, C.T. Liu, J. Appl. Phys. 109 (2011) 103505.
[50] Y. Zhang, Y.J. Zhou, J.P. Lin, G.L. Chen, P.K. Liaw, Adv. Eng. Mater. 10 (2008) 534–538.
[51] H.R. Sistla, J.W. Newkirk, F. Frank Liou, Mater. Des. 81 (2015) 113–121.
[52] S. Dasari, A. Jagetia, A. Sharma, M.S.K.K.Y. Nartu, V. Soni, B. Gwalani, S. Gorsse, R. Banerjee, Acta Mater. (2021) 116938.
[53] M.L. Lobanov, M.D. Borodina, S.V. Danilov, I.Y. Pyshmintsev, A.O. Struin, Steel Translat. 47 (2017) 710–716.
[54] J. Hou, J. Qiao, J. Lian, P.K. Liaw, Mater. Sci. Eng. A 804 (2021) 140752.
[55] L. Kubin, A. Mortensen, Scripta Mater. 48 (2003) 119.
[56] O. Muransky, L. Balogh, M. Tran, C. Hamelin, J.-S. Park, M.R. Daymond, Acta Mater. 175 (2019) 297–313.
[57] C. Haase, L.A. Barrales-Mora, Acta Mater. 150 (2018) 88–103.
[58] E. El-Danaf, S.R. Kalidindi, R.D. Doherty, C. Necker, Acta Mater. 48 (2000) 2665–2673.
[59] J. Hirsch, K. Lucke, Acta Metall. 36 (1988) 2863–2882.
[60] J.M. Park, J. Choe, J.G. Kim, J.W. Bae, J. Moon, S. Yang, K.T. Kim, J.-H. Yu, H.S. Kim, Mater. Res. Lett. 8 (2020) 1–7.
[61] S. Spriano, R. Doglione, M. Baricco, Mater. Sci. Eng. A 257 (1998) 134.
[62] Z.S. You, L. Lu, K. Lu, Acta Mater. 59 (2011) 6927–6937.
[63] L. Wang, C. Yao, J. Shen, Y. Zhang, T. Wang, Y. Ge, L. Gao, G. Zhang, Intermetallics 118 (2020) 106681.
[64] B.C. De Cooman, Y. Estrin, S.K. Kim, Acta Mater. 142 (2018) 283–362.
[65] S. Liu, Y. Wu, H. Wang, J. He, J. Liu, C. Chen, X. Liu, H. Wang, Z. Lu, Intermetallics 93 (2018) 269–273.
[66] X. Gao, Y. Lu, B. Zhang, N. Liang, G. Wu, G. Sha, J. Liu, Y. Zhao, Acta Mater. 141 (2017) 59–66.
[67] S.R. Agnew, Deformation mechanisms of magnesium alloys, in: Advances in Wrought Magnesium Alloys, Woodhead Publishing, 2012, pp. 63–104.
[68] I. Baker, F. Meng, M. Wu, A. Brandenberg, J. Alloys Compd. 656 (2016) 458–464.
[69] Z. Wang, M.C. Gao, S.G. Ma, H.J. Yang, Z.H. Wang, M. Ziomek-Moroz, J.W. Qiao, Mater. Sci. Eng. A 645 (2015) 163–169.
[70] S.G. Ma, J.W. Qiao, Z.H. Wang, H.J. Yang, Y. Zhang, Mater. Des. 88 (2015) 1057–1062.